

# Radiation-driven dusty outflows from early galaxies

Yurina Nakazato<sup>1</sup>\*, Andrea Ferrara<sup>2</sup>,

<sup>1</sup> *Department of Physics, School of Science, The University of Tokyo, Bunkyo, Tokyo 113-0033, Japan*

<sup>2</sup> *Scuola Normale Superiore, Piazza dei Cavalieri 7, 56126 Pisa, Italy*

11 December 2024

## ABSTRACT

The *James Webb Space Telescope* (JWST) has discovered an overabundance of UV-bright ( $M_{\text{UV}} \lesssim -20$ ), massive galaxies at  $z \gtrsim 10$  in comparison to pre-JWST theoretical predictions. Among the proposed interpretations, such excess has been explained by negligible dust attenuation conditions following radiation-driven outflows developing when a galaxy goes through a super-Eddington phase. Dust opacity decreases the classical Eddington luminosity by a (boost) factor  $A$ , thus favoring the driving of outflows by stellar radiation in compact, initially dusty galaxies. Here, we compute  $A$  as a function of the galaxy stellar mass, gas fraction, galaxy size, and metallicity (a total of 8 parameters). We find that the main dependence is on metallicity and, for the fiducial model,  $A \sim 1800(Z/Z_{\odot})/(1 + N_{\text{H}}/10^{23.5} \text{ cm}^{-2})$ . We apply such results to 20 spectroscopically confirmed galaxies at  $z \gtrsim 10$  and evaluate their modified Eddington ratio. We predict that three galaxies are in the outflow phase. Their outflows have relatively low velocities ( $60 - 100 \text{ km s}^{-1}$ ), implying that they are unlikely to escape from the system. For the remaining 17 galaxies that are not currently in the outflow phase, we calculate the past evolution of the modified Eddington ratio from their star formation history. We find that 15 of them experienced an outflow phase prior to observation during which they effectively displaced their dust to larger radii. Thus, radiation-driven outflows appear to be a common phenomenon among early galaxies, strongly affecting their visibility.

**Key words:** dust, extinction; galaxies: evolution; galaxies: formation; galaxies: high-redshift.

## 1 INTRODUCTION

The James Webb Space Telescope (JWST) has revolutionized our understanding of the early universe, particularly by probing galaxies at  $z > 10$  (e.g. Carniani et al. 2024a; Hainline et al. 2024a; Wang et al. 2023; Witstok et al. 2024; D’Eugenio et al. 2023; Castellano et al. 2024; Tacchella et al. 2023; Robertson et al. 2023; Atek et al. 2023; Hsiao et al. 2023; Goulding et al. 2023; Arrabal Haro et al. 2023b,a). One of the key JWST discoveries is the unexpected abundance of UV-bright, massive galaxies. In fact, multiple observational measurements of the UV luminosity function (LF) at  $z \gtrsim 10$  find a significantly larger number of bright galaxies than predicted by pre-JWST theoretical models (Harikane et al. 2024b, 2023; Finkelstein et al. 2023; Donnan et al. 2024; Pérez-González et al. 2023; McLeod et al. 2024; Yan et al. 2023).

Several solutions have been proposed to explain this tension. One possibility is a top-heavy IMF which increases the luminosity-to-stellar mass ratio compared to a bottom-heavy IMF (Inayoshi et al. 2022; Chon et al. 2022; Schaerer et al. 2024; Yung et al. 2024). Another suggestion is that galaxies could form the majority of their stars within a short timescale before the feedback becomes effective, resulting in high star formation efficiency that can account for the observed UVLF (Dekel et al. 2023; Li et al. 2023; Ceverino et al. 2024; Shuntov et al. 2024). Stochastic bursty star formation histories (SFHs) can also flatten the bright-end of the UV LF (Mason et al.

2023; Mirocha & Furlanetto 2023; Pallottini & Ferrara 2023; Shen et al. 2023; Sun et al. 2023; Gelli et al. 2024; Jeong et al. 2024).

Furthermore, modified  $\Lambda$ CDM models may alleviate the tension. Tilting the primordial power spectrum more ‘blue’ at scales  $k \gtrsim 1 \text{ h cMpc}^{-1}$ , which are not constrained by the cosmic microwave background (CMB), can increase the abundance of massive halos at  $z > 9$  (e.g. Hirano & Yoshida 2024; Parashari & Laha 2023; Ralegankar et al. 2024). Some studies also propose the presence of primordial black holes (PBHs) could explain the excess of massive halos (Liu & Bromm 2022; Colazo et al. 2024; Huang et al. 2024; Zhang et al. 2024).

Another potential solution involves dusty outflows that can displace dust on larger radii, thus decreasing the dust optical depth at the same time, making galaxies brighter and bluer (Ferrara et al. 2023; Ferrara 2024b; Tsuna et al. 2023; Fiore et al. 2023; Ziparo et al. 2023). These outflows are likely driven by the powerful radiation field produced by the young stellar population of these compact objects, exerting a strong radiation pressure on the coupled dust-gas interstellar medium. This process resembles the analog one at work in quasar outflows, which results from the super-Eddington luminosity of the central source such as an accreting black hole for quasars and local star-forming regions (e.g. Murray et al. 2005; Blackstone & Thompson 2023).

While the Eddington ratio has traditionally been used as a criterion for radiation-driven outflows, the classical Eddington luminosity assumes pure hydrogen gas, an optically thin medium to Thomson scattering, and considers only gravity from the central source. However, the vigorous star formation in compact galaxies at  $z > 10$

\* Contact e-mail: [yurina.nakazato@phys.s.u-tokyo.ac.jp](mailto:yurina.nakazato@phys.s.u-tokyo.ac.jp)

produces considerable amounts of dust, whose absorption and scattering of UV photons must be taken into account. Also, recent JWST observations report high gas column densities of high-redshift galaxies (e.g. Heintz et al. 2024; Hainline et al. 2024a; D'Eugenio et al. 2023), implying that the gravity of the surrounding gas cannot be ignored.

To account for these factors, the concept of a modified Eddington luminosity has been introduced, which incorporates dust opacity effects. Fabian et al. (2006) showed that the radiation pressure on a dusty gas can decrease the Eddington luminosity, thereby boosting the Eddington ratio. This boost factor has primarily been calculated in the context of black hole feedback from AGN (Fabian et al. 2006, 2008; Arakawa et al. 2022; Ishibashi & Fabian 2015).

In this study, we extend this approach by calculating the modified Eddington luminosity under conditions that cover the physical properties of compact galaxies at  $z > 10$ . We derive the corresponding boost factor  $A$  to quantify the increase in the Eddington ratio. Finally, we apply this boost factor to observed galaxies at  $z > 10$ .

The outline of the paper is as follows. Section 2 summarizes the analytical framework of the modified Eddington luminosity and introduces the key parameters used in our analysis. Sec. 3 presents the computation of the boost factor  $A$  and shows its dependence on various parameters. In Sec. 4, we apply this calculation to the observed  $z > 10$  galaxies and investigate the onset of a dusty outflow phase. Finally, Sec. 5 gives a brief summary of the results.

## 2 METHOD

### 2.1 Basic physical arguments

#### 2.1.1 Classical Eddington Luminosity

The classical Eddington luminosity,  $L_E$ , is derived assuming spherical geometry, a pure ionized hydrogen gas, that is optically thin to Thomson scattering; gravity is from the central source only, i.e., stars in our case. Under these assumptions, we get:

$$L_E = \frac{4\pi G M_* m_p c}{\sigma_T}, \quad (1)$$

where  $m_p$  is the proton mass, and  $\sigma_T = 6.65 \times 10^{-25} \text{ cm}^2$  is the Thomson scattering cross section. Other symbols have the usual meaning. The Eddington ratio is defined as  $\lambda_E = L/L_E$ , where  $L$  is the bolometric luminosity of the galaxy.

#### 2.1.2 Modified Eddington Luminosity

Here we assume spherical geometry, ionized hydrogen gas, and dust, and consider the gravity of the central luminous source and the surrounding gas. Dust and gas are tightly coupled by viscous and Coulomb drag forces. Dust grains in the gas interact with photons of wavelength  $\lambda$  with the radiation pressure cross section per H nucleon  $\sigma_{\text{pr,d}}(\lambda)$  [ $\text{cm}^2/\text{H}$ ]. The radiative force exerted on the gas at radius  $r$  can be expressed as

$$F_{\text{R},\lambda} = \frac{L_\lambda (1 - e^{-\tau_{\text{ext}}(\lambda)}) \sigma_{\text{pr}}(\lambda)}{4\pi r^2 c}, \quad (2)$$

where  $\sigma_{\text{pr}}$  is the wavelength-dependent radiation pressure cross section including both dust radiation pressure and Thomson scattering,  $\sigma_{\text{pr}}(\lambda) = \sigma_{\text{pr,d}}(\lambda) + \sigma_T$ . In turn,  $\sigma_{\text{pr}}$  depends on the absorption and scattering cross sections per H nucleon and on the asymmetry parameter  $\langle \cos \theta \rangle$  (Weingartner & Draine 2001):

$$\sigma_{\text{pr,d}}(\lambda) = \sigma_{\text{abs,d}}(\lambda) + (1 - \langle \cos \theta \rangle_\lambda) \sigma_{\text{sca,d}}(\lambda). \quad (3)$$

The dust absorption and scattering cross sections are linearly scaled with the dust-to-gas ratio normalized to the adopted extinction curve, i.e., Milky-Way or SMC,  $\sigma_{i,d} \propto \mathcal{D}/\mathcal{D}_{\text{MW,SMC}}$ , where  $i = (\text{abs}, \text{sca})$ , and  $\mathcal{D}_{\text{MW}} = 1/165$ ,  $\mathcal{D}_{\text{SMC}} = 1/667$ . Observations also show (e.g. Rémy-Ruyer et al. 2014; Birkin et al. 2023) that the dust-to-gas ratio scales with metallicity as  $\mathcal{D} \propto (Z/Z_\odot)$ . We assume that gas metallicity is the same as the stellar one.

The cumulative extinction optical depth is defined as  $\tau_{\text{ext}}(\lambda) \equiv [\sigma_{\text{ext,d}}(\lambda) + \sigma_T] N_{\text{H}}$ , where  $\sigma_{\text{ext,d}}$  and  $N_{\text{H}}$  are dust extinction cross-section, and the gas column density, respectively.

By integrating eq. (2) over the wavelength, we obtain

$$F_{\text{R}} = \int F_{\text{R}}(\lambda) d\lambda \simeq \frac{L_{\text{bol}} (1 - e^{-\tau_{\text{ext}}}) \sigma_{\text{pr}}}{4\pi r^2 c}. \quad (4)$$

Since the dust cross section depends on wavelength, we have defined the spectrum-averaged cross-section  $\sigma_{\text{pr}}$ ,  $\sigma_{\text{ext}}$  by weighting it with the SED shape:

$$\sigma_{\text{pr}} = \frac{\int \sigma_{\text{pr,d}}(\lambda) L_\lambda d\lambda}{\int L_\lambda d\lambda} + \sigma_T, \quad \sigma_{\text{ext}} = \frac{\int \sigma_{\text{ext,d}}(\lambda) L_\lambda d\lambda}{\int L_\lambda d\lambda} + \sigma_T, \quad (5)$$

The gravity force on a proton originates from the central stars and the surrounding gas;

$$F_{\text{G}} = F_{\text{G,star}} + F_{\text{G,gas}} = \frac{G M_* m_p}{r^2} + F_{\text{G,gas}}. \quad (6)$$

The gas gravity varies depending on gas distribution. Here we consider two density distributions: a (i) uniform sphere, and a (ii) shell.

Then we derive the modified Eddington luminosity at  $F_{\text{R}} = F_{\text{G}}$  using eq. (4) and (6);

$$L_{\text{E,mod}} = \frac{4\pi r^2 c}{(1 - e^{-\tau_{\text{ext}}}) \sigma_{\text{pr}}} F_{\text{G}} = \left( \frac{G M_* m_p}{r^2} + F_{\text{G,gas}} \right) \frac{4\pi r^2 c}{(1 - e^{-\tau_{\text{ext}}}) \sigma_{\text{pr}}}, \quad (7)$$

where

$$F_{\text{G,gas}} = \frac{4\pi G m_p^2 r n_{\text{H}}}{3} = \frac{4\pi G m_p^2 N_{\text{H}}}{3} \quad (\text{uniform}) \quad (8)$$

$$F_{\text{G,gas}} = \frac{4\pi}{3} (r^3 - r_{\text{in}}^3) n_{\text{H}} m_p \frac{G m_p}{r^2} \simeq \frac{4\pi G m_p^2 r n_{\text{H}}}{3} \left[ 1 - 3 \left( \frac{r_{\text{in}}}{r} \right) \right] \quad (\text{shell, for } r_{\text{in}} \ll r) \quad (9)$$

The boost factor is defined as  $A \equiv L_E/L_{\text{E,mod}}$ . From this definition, and using eq. (1) and eq. (7), it follows that

$$A \equiv \frac{L_E}{L_{\text{E,mod}}} = \frac{F_{\text{G,star}}}{F_{\text{G}}} \frac{(1 - e^{-\tau_{\text{ext}}}) \sigma_{\text{pr}}}{\sigma_T}. \quad (10)$$

### 2.2 Parameter setup

In order to calculate  $A$ , we set several parameters for the following three components: stellar, gas, and dust. We assume that stars are located in the central region and have total mass  $M_*$ . The gas mass is obtained by assigning the gas fraction  $f_{\text{gas}} \equiv M_{\text{gas}}/(M_{\text{gas}} + M_*)$ ; such mass is distributed within the effective radius ( $r_e$ ) according to one of the three prescribed spatial distributions (distribution), from which we obtain the gas number density  $n_{\text{H}}$ . For the shell geometry, we assume an inner radius of  $r_{\text{in}} = 0.7(0.1) \text{ pc}$ .

For the dust component, we assume Milky Way (MW) or Small Magellanic Cloud (SMC)-like dust (dust type). We employ BPASS

parameter	values	fiducial
$M_* [M_\odot]$	$10^7, 10^8, 10^9$	$10^8$
$f_{\text{gas}}$	0.33, 0.50, 0.67, 0.75	0.67
$r_e$ [pc]	50, 100, 200, 300, 400, 500	100
distribution	uniform, shell,	uniform
dust type	MW, SMC	MW
$\mathcal{D}$	$\mathcal{D}_{\text{MW}}(Z/Z_\odot)$	1/1650
age [Myr]	10, 30, 50, 100	10
$Z$	$10^{-5}, 10^{-4}, 10^{-3}, 0.002, 0.003,$ $0.004, 0.006, 0.008, 0.01, 0.02(Z_\odot)$	0.002

**Table 1.** Parameter setting. The gas fraction  $f_{\text{gas}}$  is defined as  $f_{\text{gas}} \equiv M_{\text{gas}}/(M_{\text{gas}} + M_*)$ . We assume the gas metallicity to be equal to the stellar metallicity.

SED v.2.3 (Eldridge et al. 2017; Byrne et al. 2022) and broken-power law IMF

$$N(M < M_{\text{max}}) \propto \int_{0.1}^{M_1} \left(\frac{M}{M_\odot}\right)^{\alpha_1} dM + M_1^{\alpha_1} \int_{M_1}^{M_{\text{up}}} \left(\frac{M}{M_\odot}\right)^{\alpha_2} dM, \quad (11)$$

where  $\alpha_1 = -1.3, \alpha_2 = -2.35, M_1 = 0.5 M_\odot, M_{\text{up}} = 300 M_\odot$ . We parametrize age and metallicity ( $Z$ ). We assume the obtained SED shape corresponds to bursty star formation and single stellar evolution.

Table 1 shows the parameters we set to obtain the boost factor A. The third column represents the fiducial values. The values of stellar mass, effective radius, age, and metallicity are typical ones of observed  $z > 10$  galaxies (e.g. Carniani et al. 2024a; Hainline et al. 2024a, see the references in Table 2). The average cross-sections of the fiducial model are

$$\sigma_{\text{ex}} = 1.6 \times 10^{-21} \text{ cm}^{-2} (Z/Z_\odot) \quad (12)$$

$$\sigma_{\text{pr}} = 1.2 \times 10^{-21} \text{ cm}^{-2} (Z/Z_\odot). \quad (13)$$

In this study, we assume ionized gas, i.e.,  $N_e \approx N_{\text{H}}$ . Since the cross-section of dusty gas mainly depends on the dust cross-section rather than that of the Thomson cross-section, the result does not change largely in the case of partially ionized gas.

Figure 1 shows the gravity force acting on a proton due to the stellar and gas mass distribution as a function of radius. We adopt the fiducial value for each parameter as shown in Table 1. We see that gas gravity exceeds stellar gravity at  $R \gtrsim 70(85)$  pc in the case of uniform (shell) geometry of the gas distribution.

## 3 RESULTS

### 3.1 Radial dependence of the boost factor

Figure 2 shows the boost factor as a function of the distance from the center. We describe below the behavior in three different regimes.

#### 3.1.1 Optically thin regime

Within the region of 1% of the radius, the optical depth is small and the gas mass is negligible. The gravity and radiative force are approximated as follows:

$$F_{\text{G}} \sim F_{\text{G,star}} \quad (14)$$

$$F_{\text{R}} \sim \frac{L\sigma_{\text{pr}}\tau_{\text{ext}}}{4\pi r^2 c}. \quad (15)$$

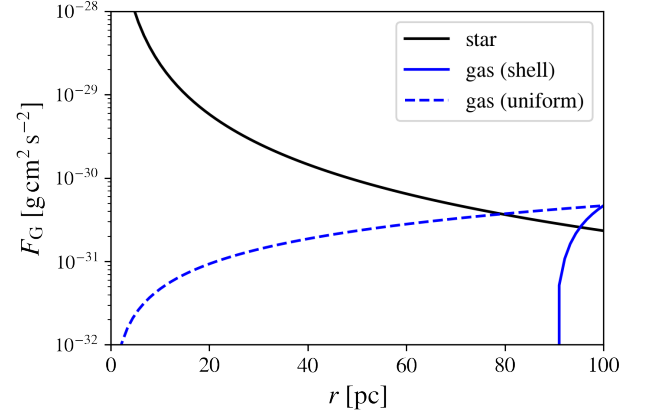


**Figure 1.** Force acting on one proton as a function of radius. We set the fiducial values written in the Table 1;  $r_e = 100$  pc,  $f_{\text{gas}} = 2/3$ ,  $M_* = 10^8 M_\odot$ . For the shell geometry, we adopt  $r_{\text{in}} = 0.7r_e$ . The black solid line shows the gravity from the central stellar components. The blue dashed (solid) line represents the gravity from the surrounding gas with uniform (shell) geometry.

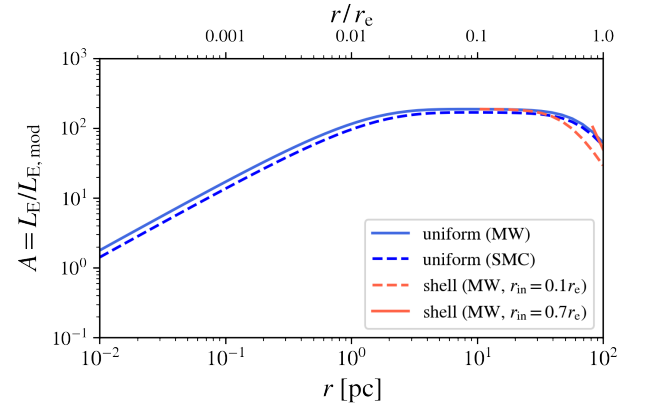


**Figure 2.** Boost factor as a function of distance from the center. The blue solid (dashed) line represents the case of a uniform gas geometry with MW (SMC)-like dust type. The red solid and dashed lines are the cases of shell gas geometry with the same dust type (MW) but with a different inner radius of  $r_{\text{in}} = 0.1r_e$  and  $0.7r_e$ , respectively. The other parameter settings ( $M_*, f_{\text{gas}}, r_e, \text{age}, Z$ ) are set as the fiducial ones in Table 1.

The modified Eddington luminosity and the boost factor becomes

$$L_{\text{E,mod}} \approx \frac{\sigma_{\text{T}}}{\sigma_{\text{pr}}\tau_{\text{ext}}} L_{\text{E}} \quad (16)$$

$$A = \frac{\sigma_{\text{pr}}\tau_{\text{ext}}}{\sigma_{\text{T}}} = \frac{\sigma_{\text{pr}}\sigma_{\text{ext}}N_{\text{H}}}{\sigma_{\text{T}}} \propto r. \quad (17)$$

#### 3.1.2 Transition regime

As the distance from the center increases to  $\gtrsim 5\%$  of the radius, the optical depth becomes  $\sim 1$ , and the gas gravity is still negligible. The gravity is the same as eq. (14) and the radiative force is

$$F_{\text{R}} \sim \frac{L\sigma_{\text{pr}}}{4\pi r^2 c}. \quad (18)$$

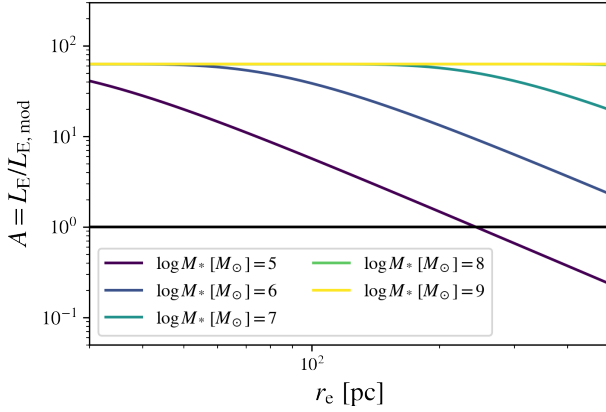


**Figure 3.** Boost factor as a function of the galaxy effective radius. The other parameters (gas fraction, age, metallicity and dust type) are fixed to their fiducial values shown in Table 1.

The modified Eddington luminosity and the boost factor are written as

$$L_{E,\text{mod}} \simeq \frac{\sigma_{\text{T}}}{\sigma_{\text{pr}}} L_{\text{E}} \quad (19)$$

$$A = \frac{\sigma_{\text{pr}}}{\sigma_{\text{T}}} = \frac{\sigma_{\text{pr,d}} + \sigma_{\text{T}}}{\sigma_{\text{T}}} \simeq \frac{\sigma_{\text{pr,d}}}{\sigma_{\text{T}}} = 1800 \left( \frac{Z}{Z_{\odot}} \right). \quad (20)$$

### 3.1.3 Optically thick regime

As the distance further increases to  $\geq 70\%$  of the radius, the gas becomes optically thick ( $\tau_{\text{ext}} \gg 1$ ), and gas gravity can no longer be neglected, as shown in Figure 1. The radiative force is still given by eq. (18), while  $F_{\text{G}} \sim F_{\text{G,gas}}$ . The boost factor is then

$$A = \frac{M_*}{M_{\text{gas}}(< r)} \frac{\sigma_{\text{pr}}}{\sigma_{\text{T}}} \quad (21)$$

$$= \begin{cases} \left[ 1 + \frac{f_{\text{gas}}}{1-f_{\text{gas}}} \left( \frac{r}{r_{\text{e}}} \right)^3 \right]^{-1} \frac{\sigma_{\text{pr}}}{\sigma_{\text{T}}} \text{ (uniform)} \\ \left[ 1 + \frac{f_{\text{gas}}}{1-f_{\text{gas}}} \left( \frac{r^3 - r_{\text{in}}^3}{r_{\text{e}}^3} \right) \right]^{-1} \frac{\sigma_{\text{pr}}}{\sigma_{\text{T}}} \text{ (shell)}. \end{cases} \quad (22)$$

Note that in this regime  $A \propto r^{-3}$  for both cases. We also change the inner radius from  $0.1r_{\text{e}}$  to  $0.9r_{\text{e}}$ , motivated by the fact that the outflow propagates through a shell-like gas geometry. Figure 2 shows the two cases of  $r_{\text{in}} = 0.1r_{\text{e}}$  and  $0.7r_{\text{e}}$  (fiducial). We find that the value of  $A$  in the shell case is the same as the one of the uniform cases at  $r \leq 0.7r_{\text{e}}$ , where the gas gravity is negligible. At  $r \geq 0.7r_{\text{e}}$  the shell geometry reduces the values of  $A$  by up to a factor of 3 compared to the uniform case. From here onwards, we concentrate on the uniform density case.

## 3.2 Parameter dependence

In this Section, we investigate the dependence of the boost factor on several physical properties: the galaxy size ( $r_{\text{e}}$ ), gas fraction  $f_{\text{gas}} (\equiv M_{\text{gas}} / (M_{\text{gas}} + M_*))$ , metallicity ( $Z$ ), stellar age (age), and dust properties as shown in Table 1.

### 3.2.1 Dependence on galaxy size

Figure 3 shows the boost factor as a function of effective radius from  $r_{\text{e}} = 50$  pc to 500 pc with different stellar masses ( $\log_{10} M_* [M_{\odot}] =$

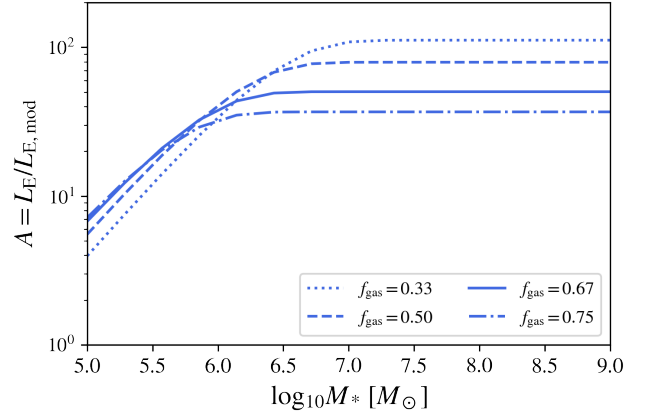


**Figure 4.** Boost factor as a function of stellar mass. Purple, blue, and green lines represent different gas geometry. The dotted, dashed, solid, and dash-dot lines show  $f_{\text{gas}} = 0.33, 0.50, 0.67$  (default),  $0.75$ , respectively.

5 – 9). For the case with  $M_* = 10^5 M_{\odot}$ ,  $f_{\text{gas}} = 0.67$ , the gas mass is  $M_{\text{gas}} = f_{\text{gas}} M_* / (1 - f_{\text{gas}}) = 2 \times 10^5 M_{\odot}$ , and the corresponding gas column density is  $\sim 10^{20.5} \text{ cm}^{-2} (M_* / 10^5 M_{\odot}) (r_{\text{e}} / 100 \text{ pc})^{-2}$ . Therefore, the gas is optically thin and  $A$  is calculated from eq. (10),

$$A = \frac{M_*}{M_* + M_{\text{gas}}} \frac{\tau_{\text{ext}} \sigma_{\text{pr}}}{\sigma_{\text{T}}} = (1 - f_{\text{gas}}) \frac{\sigma_{\text{ext}} \sigma_{\text{pr}} N_{\text{H}}}{\sigma_{\text{T}}} \sim \frac{\sigma_{\text{ext}} \sigma_{\text{pr}}}{\sigma_{\text{T}}} \frac{f_{\text{gas}} M_*}{4\pi r_{\text{e}}^2} \propto r_{\text{e}}^{-2}. \quad (23)$$

Here we use  $N_{\text{H}} \sim M_{\text{gas}} / 4\pi r_{\text{e}}^2 = f_{\text{gas}} M_* / \{4\pi r_{\text{e}}^2 (1 - f_{\text{gas}})\}$ . As the stellar and gas masses increase, gas is optically thick and  $A$  is calculated as

$$A = (1 - f_{\text{gas}}) \frac{\sigma_{\text{pr}}}{\sigma_{\text{T}}} = \text{const.} \quad (24)$$

### 3.2.2 Dependence on stellar mass/gas fraction

We also check the dependence of stellar mass and the gas fraction ( $f_{\text{gas}}$ ). Figure 4 shows the boost factors as a function of stellar mass with different  $f_{\text{gas}}$ . We see that in all cases, boost factors decrease as stellar masses decrease due to a weaker radiation pressure. For  $M_* \lesssim 10^{6.0} M_{\odot}$ , the boost factor  $A$  is written as the same as eq. (23),

$$A \sim \frac{\sigma_{\text{ext}} \sigma_{\text{pr}}}{\sigma_{\text{T}}} \frac{f_{\text{gas}} M_*}{4\pi r_{\text{e}}^2} \propto f_{\text{gas}} M_* \quad (25)$$

Therefore, when the gas is optically thin,  $A$  is proportional to the gas fraction and the stellar mass. When the stellar mass increases and the surrounding gas becomes optically thick, the boost factor becomes constant with respect to the stellar mass but inversely proportional to gas fraction, as shown in eq. (24). Figure 4 shows that the dependence of  $A$  on the gas fraction reverses around a stellar mass of  $M_* \sim 10^{6.5} M_{\odot}$ .

### 3.2.3 Dependence on metallicity

We further investigate the dependence of the boost factor on the metallicity. Figure 5 represents the boost factors as a function of metallicity with different stellar ages. From the above discussions,

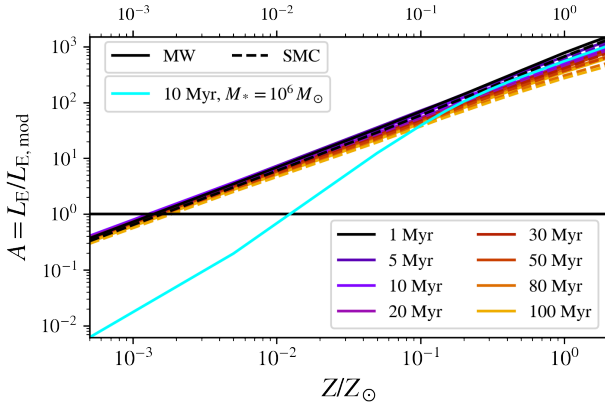


**Figure 5.** Boost factor as a function of metallicity. Solid (dashed) lines are in the case of MW (SMC) dust. Colors represent different stellar ages. We adopt the default values of stellar mass ( $M_* = 10^8 M_\odot$ ), gas fraction, radius, and stellar age in Table 1. The cyan line represents the case with a smaller stellar mass of  $M_* = 10^6 M_\odot$ .

gas is optically thick for the fiducial stellar mass and gas fraction, and  $A$  is written in the same way as eq. (24),

$$A = (1 - f_{\text{gas}}) \frac{\sigma_{\text{pr}}}{\sigma_{\text{T}}} \propto \frac{\sigma_{\text{pr,d}} + \sigma_{\text{T}}}{\sigma_{\text{T}}} \sim \frac{\sigma_{\text{pr,d}}}{\sigma_{\text{T}}} \propto Z. \quad (26)$$

The boost factor is proportional to metallicity, as shown in Figure 5. We have also plotted the case with a stellar mass of  $M_* = 10^6 M_\odot$  as a cyan solid line. In this case, gas is optically thin and  $A$  is calculated as the same as eq. (23) and eq. (25),

$$A \sim \frac{\sigma_{\text{pr}} \sigma_{\text{ext}}}{\sigma_{\text{T}}} \frac{f_{\text{gas}} M_*}{r_e^2} \propto M_* Z^2. \quad (27)$$

### 3.2.4 Dependence on stellar age

We investigate boost factors for different stellar ages of SEDs. As stellar age increases, the SEDs become softer (e.g. Xiao et al. 2018), leading to a smaller spectrum-averaged cross section  $\sigma_{\text{pr}}$  (eq. (5)). This results in weaker radiative pressure (eq. (4)). Figure 5 illustrates the boost factors for various stellar ages. The boost factors decrease with increasing stellar age, but the change is limited to a factor of  $\lesssim 2$  for all the gas distributions considered.

### 3.2.5 Dependence on dust properties

We finally investigate the dependence on the dust properties, such as the grain size distribution and composition, resulting in different absorption and scattering efficiencies (e.g. Draine 2011). We use models from Weingartner & Draine (2001) that are appropriate for MW and SMC extinction curves. The exact nature of the dust grains in high-redshift galaxies is a matter of ongoing debate (e.g. Markov et al. 2023, 2024). As the dashed lines in Figure 5 show, the boost factor  $A$  for SMC-dust differs only by a factor of  $\sim 1.1$  with respect to MW-dust cases. This is because the spectrum-averaged cross-section  $\sigma_{\text{pr}}$  is dominated by the value in the UV range, i.e.,  $\sigma_{\text{pr}} \sim \sigma_{\text{pr,UV}}$ , where the MW and SMC curves have a similar value,  $\sigma_{\text{pr,UV(MW)}} = 8.7 \times 10^{-22} \text{ cm}^2 (Z/Z_\odot)$  and  $\sigma_{\text{pr,UV(SMC)}} = 9.2 \times 10^{-22} \text{ cm}^2 (Z/Z_\odot)$ , respectively.

### 3.3 Boost factor as a function of $N_{\text{H}}$ and $Z$

According to section 3.2, we find that the dependence of the boost factor on dust type and stellar age is small and can be neglected. On the other hand, the dependencies on  $M_*$ ,  $f_{\text{gas}}$ , and  $r_e$  can be consolidated into the gas column density as  $N_{\text{H}}$  is a function of these three quantities (see eq. (23)). Hence, we conclude that  $A$  is essentially a function of  $N_{\text{H}}$  and  $Z$  only. Such relation is shown in Fig. 6, which can then be considered as the main results of this work. The key features of the relation can be understood as follows.

From eq. (5) we see that the dust opacity largely dominates above the Thomson scattering one, i.e.

$$\begin{aligned} \sigma_{\text{ext}} &= \sigma_{\text{ext,d}} + \sigma_{\text{T}} \simeq \sigma_{\text{ext,UV}} \\ &= 1.2 \times 10^{-21} \text{ cm}^{-2} \left( \frac{Z}{Z_\odot} \right). \end{aligned} \quad (28)$$

In the optically thin regime, i.e.,  $N_{\text{H}} = 10^{16-22} \text{ cm}^{-2}$ , the gravitational contribution of gas can be neglected, leading to  $F_{\text{G}} \simeq F_{\text{G,star}}$ . From eq. (10), the boost factor simplifies to

$$A = \frac{\tau_{\text{ext}} \sigma_{\text{pr}}}{\sigma_{\text{T}}} \propto N_{\text{H}} \sigma_{\text{ext}} \sigma_{\text{pr}} \propto N_{\text{H}} Z^2, \quad (29)$$

where we have used eq. (28) above. As  $N_{\text{H}} \gtrsim 10^{21} \text{ cm}^{-2} (Z/Z_\odot)^{-1}$ , the system becomes optically thick. In this regime, the gravity due to the gas can still be neglected,  $F_{\text{G}} \simeq F_{\text{G,star}}$ , and the boost factor becomes

$$A = \frac{\sigma_{\text{pr}}}{\sigma_{\text{T}}} \propto Z. \quad (30)$$

At even larger column densities, the system becomes highly optically thick and the gas gravity exceeds the stellar gravity, i.e.,  $F_{\text{G,gas}} > F_{\text{G,star}}$ . Such threshold column density can be written as

$$N_{\text{H,thres}} = \frac{M_*}{\frac{4}{3} \pi r_e^3 m_{\text{p}}} r_e = 10^{23.5} \text{ cm}^{-2} \left( \frac{M_*}{10^8 M_\odot} \right) \left( \frac{r_e}{100 \text{ pc}} \right)^{-2}.$$

In this regime, the boost factor is given by

$$\begin{aligned} A &= \frac{F_{\text{G,star}}}{F_{\text{G,star}} + F_{\text{G,gas}}} \frac{\sigma_{\text{pr}}}{\sigma_{\text{T}}} = \left( 1 + \frac{M_{\text{gas}}}{M_*} \right)^{-1} \frac{\sigma_{\text{pr}}}{\sigma_{\text{T}}} \\ &= \left( 1 + \frac{N_{\text{H}}}{N_{\text{H,thres}}} \right)^{-1} \frac{\sigma_{\text{pr}}}{\sigma_{\text{T}}} \propto N_{\text{H}}^{-1} Z. \end{aligned} \quad (31)$$

To summarize, we can express the boost factor as a function of column density and metallicity in each regime:

$$A = \begin{cases} 2.9 \times 10^{-18} N_{\text{H}} (Z/Z_\odot)^2 & (N_{\text{H}} < N_{\text{H},\tau=1}) \\ 1.8 \times 10^3 (Z/Z_\odot) & (N_{\text{H},\tau=1} \leq N_{\text{H}} < N_{\text{H,thres}}) \\ 1.8 \times 10^3 \left( 1 + \frac{N_{\text{H}}}{N_{\text{H,thres}}} \right)^{-1} (Z/Z_\odot) & (N_{\text{H}} \geq N_{\text{H,thres}}), \end{cases} \quad (32)$$

where  $N_{\text{H},\tau=1}$  is the threshold column density at which dusty gas becomes optically thick;

$$N_{\text{H},\tau=1} = \frac{1}{\sigma_{\text{ext}}} \approx 10^{21} \text{ cm}^{-2} \left( \frac{Z}{Z_\odot} \right)^{-1}. \quad (33)$$

## 4 APPLICATION TO SUPER-EARLY GALAXIES

We now apply the boost factor calculation to JWST spectroscopically confirmed  $z > 10$  galaxies, whose properties are shown in Table 2.



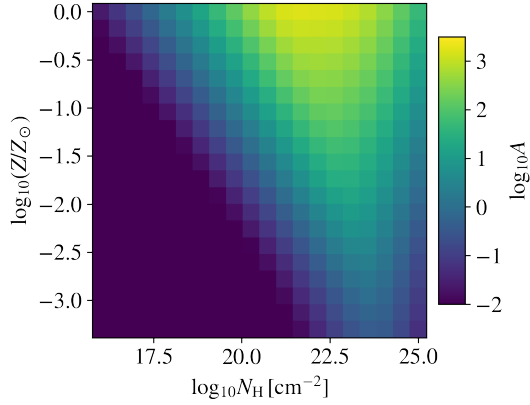


**Figure 6.** Boost factor as a function of gas column density,  $N_{\text{H}}$ , and metallicity,  $Z$ . We assume a fully ionized, pure hydrogen gas for which  $N_{\text{e}} = N_{\text{H}}$ . The other parameters are the fiducial ones in Table 1.

Based on such data, we estimate gas column density, bolometric luminosity, and the boost factor and estimate the modified Eddington ratio for each galaxy as shown in Table 3.

We estimate  $N_{\text{H}}$  from the V-band attenuation,  $A_{\text{V}}$ , as

$$N_{\text{H}} = \frac{A_{\text{V}}}{0.44\sigma_{\text{ext,UV}}} \\ = 1.9 \times 10^{23} \text{ cm}^{-2} \left( \frac{A_{\text{V}}}{0.1 \text{ mag}} \right) \left( \frac{Z}{0.1Z_{\odot}} \right)^{-1}. \quad (34)$$

The coefficient 0.44 in eq. (34) is valid for a screen geometry, i.e.,  $A_{\lambda} = 1.086\tau_{\lambda}$  and a MW extinction curve for which,  $A_{\text{UV}} = 2.46A_{\text{V}}$ <sup>1</sup>. The bolometric luminosity is calculated by BPASS using the observed values of  $M_{*}$ , age, and metallicity with an assumption of instantaneous star formation.

We find that most of the observed  $z > 10$  galaxies have the classical Eddington ratio  $\lambda_{\text{E,mod}} \simeq 10^{-3}$ . The boost factors are in the range  $1 \lesssim A \lesssim 270$ . The large  $A$  variation is induced by the metallicity scatter. In fact, as the estimated column densities are smaller than  $N_{\text{H},\tau=1}$  (optically thin regime, see eq. (33)), implying  $A \propto N_{\text{H}}Z^2$ . The modified Eddington ratios are calculated by  $\lambda_{\text{E,mod}} = A\lambda_{\text{E,class}}$ .

When assessing the onset of dusty outflow from  $\lambda_{\text{E,mod}}$ , we take into account uncertainties in the observed physical properties. Most observed  $z > 10$  galaxies lack detected emission lines, and the metallicities obtained from SED fitting are poorly constrained, often tending to be underestimated. For instance, JADES-GS-z14-0 was initially reported to have ( $Z = 0.014Z_{\odot}$ , Carniani et al. 2024a; Helton et al. 2024). However, once the [OIII] 88  $\mu\text{m}$  emission line was robustly detected by ALMA, such value has been updated to  $Z \sim 0.2Z_{\odot}$  (Carniani et al. 2024b; Schouws et al. 2024). Also, the estimated column density can increase twice when adopting an SMC dust model.

Since boost factors are highly sensitive to metallicity and column density (see eq. (32)), the actual modified Eddington ratios might be larger than the ones in Table 1 by a significant factor. Therefore, we lower the threshold for the modified Eddington ratio by a factor of 2.5, setting the new criterion to  $\lambda_{\text{E,mod}} > 0.4 (= \lambda_{\text{E,mod}}(\text{thres}))$ , and consider galaxies that meet this condition to be in the outflow phase. We find that three galaxies (GS-z12, CEERS2\_588, GN-z11) have  $\lambda_{\text{E,mod}}$  values above 0.4, with  $\lambda_{\text{E,mod}} = 1.635, 0.412, 0.457$ , respectively.

<sup>1</sup> SMC extinction curve satisfies  $A_{\text{UV}} = 5.40A_{\text{V}}$ .

For the above three galaxies, we estimate the outflow velocity as follows Thompson et al. (2015). We consider a spherical and geometrically thin dusty gas shell of mass  $M_{\text{sh}}$ . In a single-scattering momentum equation for the shell is

$$\frac{d}{dt}(M_{\text{sh}}v) = -G \frac{M_{*}M_{\text{sh}}}{r^2} + f(\tau) \frac{L_{\text{bol}}}{c} \quad (35)$$

$$f(\tau) = 1 - e^{-\tau_{\text{ext}}} + \tau_{\text{IR}} \quad (36)$$

The third term of eq. (36) comes from the momentum exchange between IR radiation and the outflowing gas. It becomes effective when the gas is optically thick to IR. We calculate the optical depth to re-radiated IR photons for the four galaxies. The values for GS-z12, CEERS2\_558, and GN-z11 are  $\tau_{\text{IR}} = 0.31, 0.35$ , and  $0.78$ , respectively, and all of the targets are optically thin to IR radiation<sup>2</sup>. Therefore, the terminal velocity is written as

$$v_{\infty} = \left( \frac{2L}{c} \right)^{1/2} \left( \frac{\kappa_{\text{UV}}}{\pi M_{\text{sh}}} \right)^{1/4} \\ = 153 \text{ kms}^{-1} \left( \frac{L}{10^{45} \text{ ergs}^{-1}} \right)^{1/2} \left( \frac{Z}{0.1Z_{\odot}} \right)^{1/4} \left( \frac{M_{\text{sh}}}{10^9 M_{\odot}} \right)^{-1/4}. \quad (37)$$

The detailed calculation is described in Appendix A.

The shell mass,  $M_{\text{sh}}$ , can be estimated from the observed  $r_{\text{e}}$  and  $N_{\text{H}}$ . We use the gas mass *just before the onset of the outflow* by assuming that it is twice as the currently observed stellar mass, i.e.,  $f_{\text{gas}} = 0.67$ . The gas fraction value within  $r_{\text{e}}$  is derived in Ziparo et al. (2023) assuming 10% of a baryonic fraction within a halo. We approximate  $M_{\text{sh}} \sim M_{\text{gas}} = f_{\text{gas}}M_{*}/(1 - f_{\text{gas}})$  following Ferrara (2024b). Substituting the values of  $L_{\text{bol}}$ ,  $M_{*}$ ,  $Z$  in Table 2 to eq. (37), we obtain  $v_{\infty} = 59, 97, 100 \text{ km s}^{-1}$  and  $V_{\text{circ}} = 70, 148, 149 \text{ km s}^{-1}$  for GS-z12, CEERS2\_588, and GN-z11, respectively. These values are 66-84% of the host halos circular velocities<sup>3</sup>, in good agreement with values inferred from observations (Xu et al. 2023; Carniani et al. 2024c).

We also calculate the dust-clearing timescale ( $t_{\text{c}}$ ) by using the outflow velocities for the three galaxies. Since the attenuation follows  $A_{\text{V}} \propto \tau_{\text{ext,UV}} \propto r^{-2}$ , we calculate  $t_{\text{c}}$  as the time it takes for the radius to expand by a factor of 10, thus decreasing  $A_{\text{V}}$  by 100 times. GS-z12, CEERS2\_588, and GN-z11 have  $t_{\text{c}} = 9r_{\text{e}}/v_{\infty} = 22, 25$ , and  $5.7 \text{ Myr}$ , respectively. As  $t_{\text{c}}$  is much shorter than the dynamical timescale, this implies that outflows can quickly clear dust once they are launched.

The other 17 observed  $z > 10$  galaxies have  $\lambda_{\text{E,mod}} \sim 10^{-3} - 0.3$ , which indicates that they are not super-Eddington at the time of the observation. However, we cannot exclude that these galaxies already went through an outflow phase at an earlier evolutionary epoch. In the following we explore such a possibility.

#### 4.1 A bursty phase prior to observation?

Ferrara (2024a) develop an analytical model for the star formation history (SFH) of high-redshift galaxies, and applied it to GS-z14-0 located at  $z = 14.32$ . Their model reproduces the physical properties of GS-z14-0 when the model galaxy becomes super-Eddington 66 Myrs

<sup>2</sup> We adopt the dust mass absorption coefficient for IR photons of  $\kappa_{\text{IR}} = 117 \text{ cm}^2 \text{ g}^{-1}$ . The derivation is described in Appendix A. We also adopt the gas mass as the twice of stellar mass.

<sup>3</sup> We derive the halo masses using the extrapolated stellar-to-halo mass relation in Behroozi et al. (2013) as the same as Scholtz et al. (2024) The obtained values are  $\log_{10} M_{\text{halo}}/M_{\odot} = 9.38, 10.4, 10.5$  for GS-z12, CEERS2\_588, and GN-z11, respectively.

Name	redshift	$\log_{10} \frac{M_*}{M_\odot}$	$r_e$ [pc]	age [Myr]	SFR [ $M_\odot/\text{yr}$ ]	$\log_{10} \frac{Z}{Z_\odot}$	$A_v$	sSFR [ $\text{Gyr}^{-1}$ ]	ref.	
1	JADES-GS-z14-0	14.32	8.7	260	10	22	-1.5	0.31	45	Carniani et al. (2024a)
2	JADES-GS-z14-1	13.9	8	160	10	2	-1.1	0.2	18	Carniani et al. (2024a)
3	GS-z13	13.2	7.7	59.3	40	1.412	-1.9	0.022	28	Hainline et al. (2024a)
4	UNCOVER-z13	13.08	8.13	309	66	1.28	-1.57	0.0434	10	Wang et al. (2023)
5	JADES-GS-z13-1-LA	13.05	7.74	61.6	21	0.16	-2.52	0.04	3	Witstok et al. (2024)
6	GS-z12	12.48	7.64	146	(10)	1.15	-0.70	0.052	26	D'Eugenio et al. (2023)
7	UNCOVER-z12	12.393	8.35	426	62	2.15	-1.34	0.21	10	Wang et al. (2023)
8	GHZ2/GLASS-z12	12.34	9.05	34	28	5.2	-1.34	0.04	5	Castellano et al. (2024)
9	Maisie	11.42	8.6	360	(10)	2	(-1)	0.1	5	Arrabal Haro et al. (2023a)
10	GS-z11	11.122	8.3	118	158	1.445	-1.9	0.043	7	Hainline et al. (2024a)
11	CEERS2_588	11.04	8.7	280	(10)	10	(-1)	0.2	20	Harikane et al. (2024b)
12	GN-z11	10.603	8.73	64	10.23	18.78	-0.92	0.17	35	Bunker et al. (2023)
13	GS-z10	10.38	7.9	(100)	31	1	(-1)	(0.1)	13	Robertson et al. (2023)
14	UNCOVER 37126	10.255	8.16	(100)	10	1.65	(-1)	(0.1)	11	Atek et al. (2023)
15	MACS0647-JD (A)	10.17	7.5	70	5	2.4	-0.70	0.01	76	Hsiao et al. (2023)
16	MACS0647-JD (B)	10.17	7.7	20	50	1	(-1)	0.13	20	Hsiao et al. (2023)
17	CEERS2_7929 (CEERS_19996)	10.1	8.66	(100)	(10)	1.9	(-1)	(0.1)	4	Arrabal Haro et al. (2023b)
18	UHZ-1 (UNCOVER 26185)	10.073	8.14	592	64.9	1.25	-0.70	0.08	9	Goulding et al. (2023)
19	CEERS_35590	10.01	9.1	420	(10)	9	(-1)	0.1	8	Arrabal Haro et al. (2023b)
20	CEERS_99715	9.97	9.5	580	(10)	6	(-1)	0.1	2	Arrabal Haro et al. (2023b)

**Table 2.** Summary of the properties of  $z > 10$  galaxies spectroscopically confirmed by JWST. **Note.** (1) Object name. (2) Redshift determined by Lyman break or rest-frame optical lines. (3) Stellar mass. (4) Effective radius. (5) Mass-weighted stellar age. (6) SFR. (7) Metallicity. (8) Dust attenuation. (9) specific SFR. (10) References. Since some physical quantities are not referenced in the literature, we adopt typical values for galaxies at  $z > 10$  and they are enclosed in parentheses.

Name	redshift	$\log_{10} N_{\text{H}}$ [ $\text{cm}^{-2}$ ]	$\log_{10} L_{\text{bol}}$ [ $\text{ergs}^{-1}$ ]	$\log_{10} L_{\text{E}}$ [ $\text{ergs}^{-1}$ ]	$\lambda_{\text{E}}$	$A$	$\lambda_{\text{E,mod}}$	
1	JADES-GS-z14-0	14.32	22.3	44.6	46.8	$6.41 \times 10^{-3}$	29.5	0.189
2	JADES-GS-z14-1	13.90	21.7	43.9	46.1	$6.32 \times 10^{-3}$	53.7	0.339
3	GS-z13	13.20	21.5	42.9	45.8	$1.23 \times 10^{-3}$	1.1	0.001
4	UNCOVER-z13	13.08	21.5	43.1	46.2	$8.01 \times 10^{-4}$	3.1	0.003
5	JADES-GS-z13-1-LA	13.05	22.8	43.3	45.8	$2.61 \times 10^{-3}$	1.4	0.004
6	GS-z12	12.48	22.1	43.5	45.7	$6.07 \times 10^{-3}$	269.2	1.635
7	UNCOVER-z12	12.39	21.9	43.4	46.4	$7.98 \times 10^{-4}$	17.4	0.014
8	GHZ2	12.34	21.2	44.4	47.1	$1.96 \times 10^{-3}$	6.3	0.012
9	Maisie	11.42	21.3	44.5	46.7	$6.28 \times 10^{-3}$	38.5	0.242
10	GS-z11	11.12	22.4	43.1	46.4	$4.72 \times 10^{-4}$	4.4	0.002
11	CEERS2_588	11.04	21.6	44.6	46.8	$6.28 \times 10^{-3}$	65.7	0.412
12	GN-z11	10.60	21.4	44.6	46.8	$6.23 \times 10^{-3}$	73.3	0.457
13	GS-z10	10.38	21.3	43.2	46.0	$1.49 \times 10^{-3}$	27.8	0.041
14	UNCOVER 37126	10.26	21.3	44.1	46.3	$6.28 \times 10^{-3}$	39.1	0.246
15	MACS0647-JD_A	10.17	20.0	43.8	45.6	$1.62 \times 10^{-2}$	10.7	0.173
16	MACS0647-JD_B	10.17	21.4	42.8	45.8	$9.17 \times 10^{-4}$	31.4	0.029
17	CEERS2_7929	10.10	21.3	44.6	46.8	$6.28 \times 10^{-3}$	39.2	0.246
18	UHZ-1	10.07	24.0	43.1	46.2	$7.24 \times 10^{-4}$	2.8	0.002
19	CEERS_35590	10.01	21.3	45.0	47.2	$6.28 \times 10^{-3}$	38.9	0.244
20	CEERS_99715	9.97	21.3	45.4	47.6	$6.28 \times 10^{-3}$	39.0	0.245

**Table 3. Notes.** (1) Object name. (2) Redshift. (3) The gas column density calculated using eq. (34). (4) Bolometric luminosity calculated from BPASS using the observed values of  $M_*$ , age, and metallicity from Table 2. (5) Classical Eddington luminosity based on  $M_*$  from Table 2. (6) Classical Eddington ratio,  $\lambda_{\text{E}} \equiv L_{\text{bol}}/L_{\text{E}}$ . (7) Boost factor. (8) Modified Eddington ratio,  $\lambda_{\text{E,mod}} = A\lambda_{\text{E}}$ .

before the observation and a dusty outflow continues for 40 Myrs. We, therefore, investigate if the observed galaxies have experienced the dusty outflow phase a few  $\times 10$  Myr before the observations. We consider the delayed- $\tau$  star formation model according to which the SFR exponentially declines with time after an initial burst occurring

at  $t = t_{\text{SF}}$ ,

$$\text{SFR}(t) \propto \begin{cases} 0 & (t < t_{\text{SF}}) \\ (t - t_{\text{SF}}) \exp\left(-\frac{t - t_{\text{SF}}}{\tau}\right) & (t > t_{\text{SF}}). \end{cases} \quad (38)$$

The corresponding evolution of the stellar mass is

$$M_*(t) = \begin{cases} 0 & (t < t_{\text{SF}}) \\ M_0 \tau \left[ \tau - (t - t_{\text{SF}} + \tau) e^{-(t-t_{\text{SF}})/\tau} \right] & (t > t_{\text{SF}}), \end{cases} \quad (39)$$

$$M_0 = \frac{M_*(t_{\text{obs}})}{\tau \left[ \tau - (\tau_{\text{age}} + \tau) e^{-\tau_{\text{age}}/\tau} \right]}, \quad (40)$$

where  $\tau_{\text{age}} = t_{\text{obs}} - t_{\text{SF}}$  is roughly equal to mass-weighted stellar age obtained from observation (Table 2). The constant  $M_0$  is obtained by imposing  $\int \text{SFR}(t) dt = M_*(t_{\text{obs}})$ . For typical star formation timescale  $\tau$ , we assume  $\tau = 2$  Myr, which is the free-fall time at  $n_{\text{H}} \sim 10^3 \text{ cm}^{-3}$ . We assume that galaxy sizes do not change largely and set  $r_e(t) = r_e(t_{\text{obs}})$ . For metallicity, we set

$$Z(t) = Z(t_{\text{obs}}) \left( \frac{M_*(t)}{M_*(t_{\text{obs}})} \right)^x, \quad (41)$$

where the power  $x = 0.3 - 0.5$  is the slope of the mass-metallicity relation inferred from recent observations and theoretical studies at  $z \gtrsim 9$  (e.g. Nakajima et al. 2023; Nakazato et al. 2023; Langan et al. 2020; Tsuna et al. 2023); we adopt  $x = 0.5$ . We assume that the initial gas mass is twice as the observed stellar mass, i.e.,  $M_{\text{gas}}(t) = 2M_*(t_{\text{obs}}) - M_*(t)$ . The bolometric luminosity is derived as  $L_{\text{bol}} = f_{\text{bol}} L_{\text{UV}}$ , where  $f_{\text{bol}} = 2$  (Fiore et al. 2023), is a bolometric correction, and  $L_{\text{UV}}$  is the intrinsic UV luminosity computed as  $L_{\text{UV}} = \mathcal{K}_{\text{UV}} \text{SFR}$ . Here  $\mathcal{K}_{\text{UV}}$  is a conversion factor and its value is chosen to match the one used by the ALMA REBELS survey  $\mathcal{K}_{\text{UV}} = 0.587 \times 10^{10} L_{\odot} / M_{\odot} \text{ yr}^{-1}$  (Bouwens et al. 2022).

Figure 7 shows the time evolution of  $A$  (left) and modified Eddington ratios (right) for the other 17 galaxies. We find that 15 out of 17 galaxies have a phase where  $\lambda_{\text{E,mod}} \gtrsim 0.4$  and therefore should have experienced outflows before the observation. The time evolution of  $\lambda_{\text{E,mod}}$  closely tracks that of the SFR. It reaches a peak at  $t - t_{\text{SF}} \sim \tau = 2$  Myr. For the 15 objects exceeding the threshold, we calculate the clearing timescale,  $t_c$ , as defined in Section 4 by adopting the physical properties at  $t - t_{\text{SF}} = \tau$ . We find that 10 out of 15 galaxies have  $(\tau_{\text{age}} - \tau > t_c)$ , which indicates that outflows can expel the produced dust and effectively decrease  $A_{\text{V}}$  by the time of observation.

We note that in Figure 7 we see that MACS0647-JD(A) has  $\lambda_{\text{E,mod}} > 1$  at the observing phase, even though it is shown to have  $\lambda_{\text{E,mod}} < 1$  by using the observed physical properties in Table 3. This is because we adopt the delayed-tau model for all galaxies. The SFH model might not be appropriate for that system.

## 4.2 Caveats

Our model contains some approximations that are worth discussing. First, we assume a spherical gas distribution and a concentrated stellar distribution as a point source. The point-like approximation can be applicable to compact galaxies observed at  $z > 10$ . This approximation becomes more accurate as the outflow develops and the gas is spread on scales much larger than  $r_e$ . However, massive galaxies in the Epoch of Reionization ( $z \sim 6 - 8$ ) with stellar masses of  $M_* \gtrsim 10^9 M_{\odot}$  are known to have more complex morphologies, such as clumpy structures or extended disks, as revealed by both observations and simulations (e.g. Chen et al. 2023; Hainline et al. 2024a,b; Rowland et al. 2024; Harikane et al. 2024a; Nakazato et al. 2024; Kohandel et al. 2024). Also, in realistic galaxies, gas and stars are well-mixed as seen in simulations (e.g. Ceverino et al. 2024; Pallottini et al. 2022). In this case, the radiative pressure from stars can become more complex, where it might not always work as an outward

pressure but as an inward pressure. We plan to treat this complex geometry in future work by performing radiation-hydrodynamical simulations.

Furthermore, we assume that dust and gas are tightly dynamically coupled. To check if this is a reasonable assumption, we compare the mean free path for grain-atom collisions and galaxy size based on Murray et al. (2005). The mean free path is  $\lambda = (n_{\text{H}} \sigma_{\text{dg}})^{-1}$ , where  $\sigma_{\text{dg}}$  is the dust-gas scattering cross section. Since we require that order of unity of the dust momentum imparted to the gas, the quantity of interest is  $\lambda_{\text{M}} = \lambda(m_{\text{D}}/m_{\text{p}})$ , where  $m_{\text{D}}$  is the mass of an individual spherical dust grain of radius  $a$ . Considering the geometric cross-section we estimate

$$\lambda_{\text{M}} = \frac{1}{n_{\text{H}} a^2 \pi} \frac{m_{\text{D}}}{m_{\text{p}}} = 7.8 \text{ pc} \left( \frac{a}{0.1 \mu\text{m}} \right) \left( \frac{n_{\text{H}}}{1 \text{ cm}^{-3}} \right)^{-1} \left( \frac{\rho_{\text{d}}}{3 \text{ g cm}^{-3}} \right), \quad (42)$$

where  $\rho_{\text{d}}$  is the mass density of dust grains.

Therefore, by comparing  $\lambda_{\text{M}}$  with the typical size of observed  $z > 10$  galaxies ( $\sim 100$  pc), we find  $\lambda_{\text{M}} \ll r_e$ . Hence, the dust is efficiently coupled with the gas, transferring the radiation field momentum to it. However, at low column densities in Figure 6), it is possible to have  $\lambda_{\text{M}} > r_e$  and thus for dust and gas to be decoupled. This scenario might allow the outflow to sweep away only the dust from the galaxy while leaving enough gas behind to support continued star formation.

## 5 SUMMARY

We have calculated the modified Eddington luminosity in a dusty medium as a function of 8 galaxy parameters: stellar mass, gas fraction, size, gas distribution, dust properties, dust-to-gas ratio, stellar age, and metallicity. We have introduced the boost factor  $A \equiv L_{\text{E}}/L_{\text{E,mod}}$ , which represents the ratio between the classical Eddington luminosity and the modified Eddington luminosity in a dusty medium.

Unlike the classical Eddington luminosity, which only considers Thomson scattering, the modified Eddington condition accounts for both the absorption and scattering of photons (primarily UV) by dust, which lowers the modified Eddington luminosity and relaxes the conditions for super-Eddington outflows to occur. The main findings are:

- The boost factor  $A$  primarily depends on gas metallicity,  $Z$ , and column density,  $N_{\text{H}}$ . This is because the dust-to-gas mass ratio scales to metallicity and the column density mainly reflects the optical depth of dusty gas and the contribution of gas gravity. Expressions for  $A$  in different optical depth regimes are given simple, but accurate expression for the boost factor is as expressed in eq. (32). For  $\tau \approx 1$ , it is  $A = 1800(Z/Z_{\odot})$ .

- We apply the above results to the 20 galaxies currently observed at  $z \gtrsim 10$  and derive both  $A$  and the modified Eddington ratio  $\lambda_{\text{E,mod}}$ . Three galaxies (GS-z12, CEERS2\_588, and GN-z11) are likely in the outflow phase, with the outflow velocities of 60-100 km s<sup>-1</sup>.

- For the other  $z > 10$  galaxies, we model their star formation histories (SFH) to check whether they have experienced an outflow phase before the observation epoch. Assuming a delayed- $\tau$  model, we find that 15/17 galaxies had  $\lambda_{\text{E,mod}} > \lambda_{\text{E,mod(thres)}} (= 0.4)$  before the observation. We estimate the dust-clearing timescale ( $t_c$ ) required to reduce  $A_{\text{V}}$  by a factor of 100 and find that 10/15 galaxies have a clearing time much shorter than their stellar ages. This implies that outflows have effectively expelled the dust prior to observation.



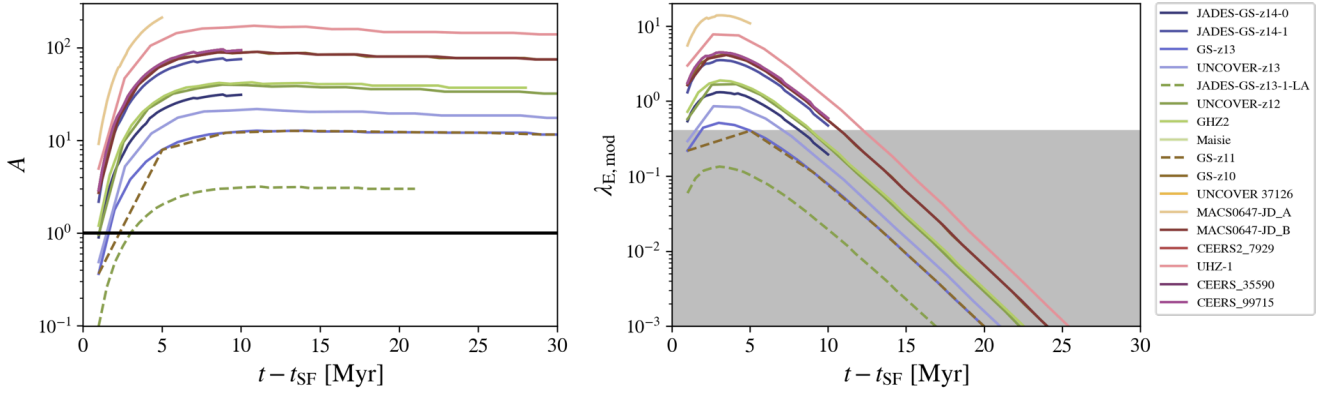


**Figure 7.** Time evolution of boost factor  $A$  (left) and the modified Eddington ratios  $\lambda_{E,\text{mod}}$  (right). The gray regions from  $\lambda_{E,\text{mod}} < 0.4$  indicate the rough boundary where dusty outflows are not onset. We plot the results of JADES-GS-z13-LA and GS-z11 as dashed lines to show they have not experienced outflow phases.

The above results highlight the possibility that radiation-driven outflows are a widespread phenomenon during the early phases of galaxy evolution probed by JWST at high redshifts. Such outflows might be crucial in shaping the observed properties of these systems and in regulating their evolution. The investigation of such issues will require future dedicated theoretical and numerical modeling.

## ACKNOWLEDGEMENTS

We thank N. Yoshida, Y. Harikane, T. Hosokawa, M. Ouchi, K. Omukai, H. Yajima, H. Fukushima for useful discussions. YN acknowledges funding from JSPS KAKENHI Grant Number 23KJ0728, JSPS International Leading Research 23K20035, and JSR fellowship. AF acknowledges support from the ERC Advanced Grant INTERSTELLAR H2020/740120. Partial support from the Carl Friedrich von Siemens-Forschungspreis der Alexander von Humboldt-Stiftung Research Award is kindly acknowledged. This research was supported in part by grant NSF PHY-2309135 to the Kavli Institute for Theoretical Physics (KITP). This work made use of v2.3 of the Binary Population and Spectral Synthesis (BPASS) models as described in [Byrne et al. \(2022\)](#) and [Stanway & Eldridge \(2018\)](#).

## DATA AVAILABILITY

All data underlying this article are available on reasonable request to the corresponding author.

## REFERENCES

- Arakawa N., Fabian A. C., Ferland G. J., Ishibashi W., 2022, *MNRAS*, **517**, 5069
- Arrabal Haro P., et al., 2023a, *Nature*, **622**, 707
- Arrabal Haro P., et al., 2023b, *ApJ*, **951**, L22
- Atek H., et al., 2023, *MNRAS*, **524**, 5486
- Behroozi P. S., Wechsler R. H., Conroy C., 2013, *ApJ*, **770**, 57
- Birkin J. E., et al., 2023, *ApJ*, **958**, 64
- Blackstone I., Thompson T. A., 2023, *MNRAS*, **523**, 4309
- Bouwens R. J., et al., 2022, *ApJ*, **931**, 160
- Bunker A. J., et al., 2023, *A&A*, **677**, A88
- Byrne C. M., Stanway E. R., Eldridge J. J., McSwiney L., Townsend O. T., 2022, *MNRAS*, **512**, 5329
- Carniani S., et al., 2024a, *arXiv e-prints*, p. [arXiv:2405.18485](#)
- Carniani S., et al., 2024b, *arXiv e-prints*, p. [arXiv:2409.20533](#)
- Carniani S., et al., 2024c, *A&A*, **685**, A99
- Castellano M., et al., 2024, *arXiv e-prints*, p. [arXiv:2403.10238](#)
- Ceverino D., Nakazato Y., Yoshida N., Klessen R., Glover S., 2024, *arXiv e-prints*, p. [arXiv:2404.02537](#)
- Chen Z., Stark D. P., Endsley R., Topping M., Whittler L., Charlot S., 2023, *MNRAS*, **518**, 5607
- Chon S., Ono H., Omukai K., Schneider R., 2022, *MNRAS*, **514**, 4639
- Colazo P. E., Staszczyn F., Padilla N., 2024, *A&A*, **685**, L8
- D’Eugenio F., et al., 2023, *arXiv e-prints*, p. [arXiv:2311.09908](#)
- Dekel A., Sarkar K. C., Birnboim Y., Mandelker N., Li Z., 2023, *MNRAS*, **523**, 3201
- Donnan C. T., et al., 2024, *MNRAS*, **533**, 3222
- Draine B. T., 2011, *Physics of the Interstellar and Intergalactic Medium*
- Eldridge J. J., Stanway E. R., Xiao L., McClelland L. A. S., Taylor G., Ng M., Greis S. M. L., Bray J. C., 2017, *Publ. Astron. Soc. Australia*, **34**, e058
- Fabian A. C., Celotti A., Erlund M. C., 2006, *MNRAS*, **373**, L16
- Fabian A. C., Vasudevan R. V., Gandhi P., 2008, *MNRAS*, **385**, L43
- Ferrara A., 2024a, *arXiv e-prints*, p. [arXiv:2405.20370](#)
- Ferrara A., 2024b, *A&A*, **684**, A207
- Ferrara A., et al., 2022, *MNRAS*, **512**, 58
- Ferrara A., Pallottini A., Dayal P., 2023, *MNRAS*, **522**, 3986
- Finkelstein S. L., et al., 2023, *ApJ*, **946**, L13
- Fiore F., Ferrara A., Bischetti M., Feruglio C., Travascio A., 2023, *ApJ*, **943**, L27
- Gelli V., Mason C., Hayward C. C., 2024, *arXiv e-prints*, p. [arXiv:2405.13108](#)
- Goulding A. D., et al., 2023, *ApJ*, **955**, L24
- Hainline K. N., et al., 2024a, *arXiv e-prints*, p. [arXiv:2404.04325](#)
- Hainline K. N., et al., 2024b, *ApJ*, **964**, 71
- Harikane Y., et al., 2023, *ApJS*, **265**, 5
- Harikane Y., et al., 2024a, *arXiv e-prints*, p. [arXiv:2406.18352](#)
- Harikane Y., Nakajima K., Ouchi M., Umeda H., Isobe Y., Ono Y., Xu Y., Zhang Y., 2024b, *ApJ*, **960**, 56
- Heintz K. E., et al., 2024, *Science*, **384**, 890
- Helton J. M., et al., 2024, *arXiv e-prints*, p. [arXiv:2405.18462](#)
- Hirano S., Yoshida N., 2024, *ApJ*, **963**, 2
- Hsiao T. Y.-Y., et al., 2023, *arXiv e-prints*, p. [arXiv:2305.03042](#)
- Huang H.-L., Jiang J.-Q., Piao Y.-S., 2024, *arXiv e-prints*, p. [arXiv:2407.15781](#)
- Inayoshi K., Harikane Y., Inoue A. K., Li W., Ho L. C., 2022, *ApJ*, **938**, L10
- Ishibashi W., Fabian A. C., 2015, *MNRAS*, **451**, 93
- Jeong T. B., Jeon M., Song H., Bromm V., 2024, *arXiv e-prints*, p. [arXiv:2411.17007](#)
- Kohandel M., Pallottini A., Ferrara A., Zanella A., Rizzo F., Carniani S., 2024, *A&A*, **685**, A72
- Langan I., Ceverino D., Finlator K., 2020, *MNRAS*, **494**, 1988

- Li Z., Dekel A., Sarkar K. C., Aung H., Gialalisco M., Mandelker N., Tacchella S., 2023, [arXiv e-prints](#), p. [arXiv:2311.14662](#)
- Liu B., Bromm V., 2022, [ApJ](#), **937**, L30
- Markov V., Gallerani S., Pallottini A., Sommovigo L., Carniani S., Ferrara A., Parlanti E., Di Mascia F., 2023, [A&A](#), **679**, A12
- Markov V., Gallerani S., Ferrara A., Pallottini A., Parlanti E., Di Mascia F., Sommovigo L., Kohandel M., 2024, [arXiv e-prints](#), p. [arXiv:2402.05996](#)
- Mason C. A., Trenti M., Treu T., 2023, [MNRAS](#), **521**, 497
- McLeod D. J., et al., 2024, [MNRAS](#), **527**, 5004
- Mirocha J., Furlanetto S. R., 2023, [MNRAS](#), **519**, 843
- Murray N., Quataert E., Thompson T. A., 2005, [ApJ](#), **618**, 569
- Nakajima K., Ouchi M., Isobe Y., Harikane Y., Zhang Y., Ono Y., Umeda H., Oguri M., 2023, [ApJS](#), **269**, 33
- Nakazato Y., Yoshida N., Ceverino D., 2023, [ApJ](#), **953**, 140
- Nakazato Y., Ceverino D., Yoshida N., 2024, [arXiv e-prints](#), p. [arXiv:2402.08911](#)
- Pallottini A., Ferrara A., 2023, [A&A](#), **677**, L4
- Pallottini A., et al., 2022, [MNRAS](#), **513**, 5621
- Parashari P., Laha R., 2023, [MNRAS](#), **526**, L63
- Pérez-González P. G., et al., 2023, [ApJ](#), **951**, L1
- Ralegankar P., Pavičević M., Viel M., 2024, [J. Cosmology Astropart. Phys.](#), **2024**, 027
- Rémy-Ruyer A., et al., 2014, [A&A](#), **563**, A31
- Robertson B. E., et al., 2023, [Nature Astronomy](#), **7**, 611
- Rowland L. E., et al., 2024, [arXiv e-prints](#), p. [arXiv:2405.06025](#)
- Schaerer D., Guibert J., Marques-Chaves R., Martins F., 2024, [arXiv e-prints](#), p. [arXiv:2407.12122](#)
- Scholtz J., et al., 2024, [A&A](#), **687**, A283
- Schouws S., et al., 2024, [arXiv e-prints](#), p. [arXiv:2409.20549](#)
- Shen X., Vogelsberger M., Boylan-Kolchin M., Tacchella S., Kannan R., 2023, [MNRAS](#), **525**, 3254
- Shuntov M., et al., 2024, [arXiv e-prints](#), p. [arXiv:2410.08290](#)
- Sommovigo L., et al., 2022, [MNRAS](#), **513**, 3122
- Stanway E. R., Eldridge J. J., 2018, [MNRAS](#), **479**, 75
- Sun G., Faucher-Giguère C.-A., Hayward C. C., Shen X., Wetzel A., Cochrane R. K., 2023, [ApJ](#), **955**, L35
- Tacchella S., et al., 2023, [ApJ](#), **952**, 74
- Thompson T. A., Fabian A. C., Quataert E., Murray N., 2015, [MNRAS](#), **449**, 147
- Tsuna D., Nakazato Y., Hartwig T., 2023, [MNRAS](#), **526**, 4801
- Wang B., et al., 2023, [ApJ](#), **957**, L34
- Weingartner J. C., Draine B. T., 2001, [ApJ](#), **548**, 296
- Witstok J., et al., 2024, [arXiv e-prints](#), p. [arXiv:2408.16608](#)
- Xiao L., Stanway E. R., Eldridge J. J., 2018, [MNRAS](#), **477**, 904
- Xu Y., Ouchi M., Nakajima K., Harikane Y., Isobe Y., Ono Y., Umeda H., Zhang Y., 2023, [arXiv e-prints](#), p. [arXiv:2310.06614](#)
- Yan H., Ma Z., Ling C., Cheng C., Huang J.-S., 2023, [ApJ](#), **942**, L9
- Yung L. Y. A., Somerville R. S., Finkelstein S. L., Wilkins S. M., Gardner J. P., 2024, [MNRAS](#), **527**, 5929
- Zhang S., Bromm V., Liu B., 2024, [arXiv e-prints](#), p. [arXiv:2405.11381](#)
- Ziparo F., Ferrara A., Sommovigo L., Kohandel M., 2023, [MNRAS](#), **520**, 2445

## APPENDIX A: CALCULATION OF TERMINAL VELOCITY

Here we derive the terminal velocity  $v_\infty$  based on [Thompson et al. \(2015\)](#). We first assume that the mass of the shell is constant as a function of radius (i.e., the shell expands into vacuum.) The general expression for momentum conservation for a thin shell of mass  $M_{\text{sh}}$  is

$$\frac{d}{dt}(M_{\text{sh}}v) = -G \frac{M_* M_{\text{sh}}}{r^2} + (1 - e^{-\tau_{\text{UV}}} + \tau_{\text{IR}}) \frac{L_{\text{bol}}}{c} M_{\text{sh}} \quad (\text{A1})$$

$$\therefore \frac{dv}{dr} = -G \frac{M_* M_{\text{sh}}}{r^2} + (1 - e^{-\tau_{\text{UV}}} + \tau_{\text{IR}}) \frac{L_{\text{bol}}}{c} \quad (\text{A2})$$

where  $\tau_{\text{UV,IR}}$  is the optical depth of the shell to UV(IR) photons;

$$\tau_{\text{UV,IR}} = \frac{\kappa_{\text{UV,IR}} M_{\text{sh}}}{4\pi r^2}. \quad (\text{A3})$$

Here  $\kappa_{\text{UV,IR}}$  is the dust mass absorption coefficient for UV (IR) photons. Adopting a MW extinction with a dust-to-gas ratio  $\mathcal{D}_{\text{MW}} = 1/165$ , the value at  $1500 \text{ \AA}$  is  $\kappa_{\text{UV}} = \kappa_{1500} = 1.26 \times 10^5 \text{ cm}^2 \text{ g}^{-1} (\mathcal{D}/\mathcal{D}_{\text{MW}})$  ([Ferrara et al. 2022](#)). For the IR coefficient,  $\kappa_{\text{IR}}(\nu) = \kappa_{158} (\nu/\nu_{158})^{\beta_{\text{d}}}$ , is pivoted at wavelength  $\lambda = 158 \mu\text{m}$ . For a MW curve,  $\kappa_{158} = 10.41 \text{ cm}^2 \text{ g}^{-1}$ , and  $\beta_{\text{d}} = 2.03$  ([Weingartner & Draine 2001](#)). Dust temperature ( $T_{\text{d}}$ ) increases as redshift is higher, and reaches values of 50-70 K at  $z \approx 10$  (e.g., [Sommovigo et al. 2022](#)). We adopt  $T_{\text{d}} = 60 \text{ K}$  as a fiducial value and compute  $\kappa_{\text{IR}}$  at the peak wavelength of the gray-body spectrum,  $\lambda_{\text{p}} = 0.29/T_{\text{d}} = 48 \mu\text{m}$ , obtaining  $\kappa_{\text{IR}}(\nu_{\text{p}}) = 117 \text{ cm}^2 \text{ g}^{-1} (\mathcal{D}/\mathcal{D}_{\text{MW}})$ . Therefore, the opacity for IR photons is over 1000 times lower than that for UV photons.

We introduce a characteristic radius,  $R_{\text{UV}}$ , at which the shell become optically thin to UV photons;

$$R_{\text{UV}} = \left( \frac{\kappa_{\text{IR}} M_{\text{sh}}}{4\pi} \right)^{1/2} = 1.9 \text{ kpc} \left( \frac{M_{\text{gas}}}{10^9 M_\odot} \right)^{1/2} \left( \frac{Z}{0.1 Z_\odot} \right)^{1/2}. \quad (\text{A4})$$

Integrating eq. (A2) from the initial distance  $R_0$  to  $R_{\text{UV}}$ , the left hand side of eq. (A2) becomes

$$\int_{R_0}^{R_{\text{UV}}} M_{\text{sh}} v \frac{dv}{dr} dr = \frac{M_{\text{sh}}}{2} (v_{\text{UV}}^2 - v_0^2). \quad (\text{A5})$$

Here  $v_{\text{UV}}, v_0$  are the velocities at  $R_{\text{UV}}, R_0$ . The right-hand side of eq. (A2) becomes

$$\begin{aligned} & \int_{R_0}^{R_{\text{UV}}} -\frac{G M M_{\text{sh}}}{r^2} dr + \int_{R_0}^{R_{\text{UV}}} (1 + \tau_{\text{IR}}) \frac{L}{c} dr \\ &= G M M_{\text{sh}} \left( \frac{1}{R_{\text{UV}}} - \frac{1}{R_0} \right) + \frac{L}{c} \left[ R_{\text{UV}} - R_0 + \frac{\kappa_{\text{IR}} M_{\text{sh}}}{4\pi} \left( \frac{1}{R_{\text{UV}}} - \frac{1}{R_0} \right) \right] \\ &= \left[ -\frac{G M M_{\text{sh}}}{R_0} + \frac{L}{c} \left( R_{\text{UV}} + \frac{\kappa_{\text{IR}} M_{\text{sh}}}{4\pi R_0} \right) \right] \left( 1 - \frac{R_0}{R_{\text{UV}}} \right). \quad (\text{A6}) \end{aligned}$$

We also integrate eq. (A2) in the regions at  $R_{\text{UV}} \leq r \leq \infty$ , where the shell is optically thin to UV photons. The left-hand side of eq. (A2) becomes

$$\frac{M_{\text{sh}}}{2} (v_\infty^2 - v_{\text{UV}}^2). \quad (\text{A7})$$

The right-hand side of eq. (A2) becomes

$$-\frac{G M M_{\text{sh}}}{R_{\text{UV}}} + \int_{R_{\text{UV}}}^{\infty} \frac{L \tau_{\text{UV}}}{c} dr = -\frac{G M M_{\text{sh}}}{R_{\text{UV}}} + \frac{L}{c} \frac{\kappa_{\text{UV}} M_{\text{sh}}}{4\pi R_{\text{UV}}}. \quad (\text{A8})$$

Therefore, integrating  $0 \leq r \leq \infty$ , the left hand side becomes

$$M_{\text{sh}} \frac{v_\infty^2}{2} - M_{\text{sh}} \frac{v_0^2}{2} \sim M_{\text{sh}} \frac{v_\infty^2}{2}. \quad (\text{A9})$$

We take the zero initial shell velocity ( $v_0 \sim 0$ ). For the right hand side, taking  $R_0 \ll R_{\text{UV}}$  and  $\kappa_{\text{IR}} \ll \kappa_{\text{UV}}$ ,

$$\begin{aligned} & \left[ -\frac{G M M_{\text{sh}}}{R_0} + \frac{L}{c} \left( R_{\text{UV}} + \frac{\kappa_{\text{IR}} M_{\text{sh}}}{4\pi R_0} \right) \right] \left( 1 - \frac{R_0}{R_{\text{UV}}} \right) + \frac{M_{\text{sh}}}{R_{\text{UV}}} \left( \frac{\kappa_{\text{UV}} L}{4\pi c} - G M \right) \\ & \approx -\frac{G M M_{\text{sh}}}{R_0} \left( 1 + \frac{R_0}{R_{\text{UV}}} \right) + \frac{L R_{\text{UV}}}{c} + \frac{M_{\text{sh}} L}{4\pi c} \frac{\kappa_{\text{UV}}}{R_{\text{UV}}} \left( 1 + \frac{\kappa_{\text{IR}}}{\kappa_{\text{UV}}} R_0 R_{\text{UV}} \right) \\ & \approx -\frac{G M M_{\text{sh}}}{R_0} + \frac{L R_{\text{UV}}}{c} + \frac{L M_{\text{sh}}}{4\pi c} \frac{\kappa_{\text{UV}}}{R_{\text{UV}}}. \quad (\text{A10}) \end{aligned}$$

Assuming that the radiative pressure term is significantly large and

the gravity term in eq.(A10) can be neglected, we obtain

$$\frac{v_\infty^2}{2} = \frac{LR_{UV}}{cM_{sh}} + \frac{L}{4\pi c} \frac{\kappa_{UV}}{R_{UV}} = \frac{L}{c} \left( \frac{\kappa_{UV}}{\pi M_{sh}} \right)^{1/2} \quad (\text{A11})$$

$$\begin{aligned} \therefore v_\infty &= \left( \frac{2L}{c} \right)^{1/2} \left( \frac{\kappa_{UV}}{\pi M_{sh}} \right)^{1/4} \\ &= 153 \text{ kms}^{-1} \left( \frac{L}{10^{45} \text{ ergs}^{-1}} \right)^{1/2} \left( \frac{Z}{0.1Z_\odot} \right)^{1/4} \left( \frac{M_{sh}}{10^9 M_\odot} \right)^{1/4}. \end{aligned} \quad (\text{A12})$$

This paper has been typeset from a  $\text{\TeX}/\text{\LaTeX}$  file prepared by the author.